Winter Precipitation Liquid–Ice Phase Transitions Revealed with Polarimetric Radar and 2DVD Observations in Central Oklahoma

PETAR BUKOVČIĆ

NOAA/National Severe Storms Laboratory, and Cooperative Institute for Mesoscale Meteorological Studies, and School of Meteorology, and Advanced Radar Research Center, University of Oklahoma, Norman, Oklahoma

DUŠAN ZRNIĆ

NOAA/National Severe Storms Laboratory, Norman, Oklahoma

GUIFU ZHANG

School of Meteorology, and Advanced Radar Research Center, University of Oklahoma, Norman, Oklahoma

(Manuscript received 30 June 2016, in final form 8 November 2016)

ABSTRACT

Observations and analysis of an ice–liquid phase precipitation event, collected with an S-band polarimetric KOUN radar and a two-dimensional video disdrometer (2DVD) in central Oklahoma on 20 January 2007, are presented. Using the disdrometer measurements, precipitation is classified either as ice pellets or rain/freezing rain. The disdrometer observations showed fast-falling and slow-falling particles of similar size. The vast majority (>99%) were fast falling with observed velocities close to those of raindrops with similar sizes. In contrast to the smaller particles (<1 mm in diameter), bigger ice pellets (>1.5 mm) were relatively easy to distinguish because their shapes differ from the raindrops. The ice pellets were challenging to detect by looking at conventional polarimetric radar data because of the localized and patchy nature of the ice phase and their occurrence close to the ground. Previously published findings referred to cases in which ice pellet areas were centered on the radar location and showed a ringlike structure of enhanced differential reflectivity Z_{DR} and reduced copolar correlation coefficient ρ_{hv} and horizontal reflectivity Z_H in PPI images. In this study, a new, unconventional way of looking at polarimetric radar data is introduced: slanted vertical profiles (SVPs) at low (0°–1°) radar elevations. From the analysis of the localized and patchy structures using SVPs, the polarimetric refreezing signature, reflected in local enhancement in Z_{DR} and reduction in Z_H and ρ_{hv}, became much more evident. Model simulations of sequential drop freezing using Marshall–Palmer DSDs along with the observations suggest that preferential freezing of small drops may be responsible for the refreezing polarimetric signature, as suggested in previous studies.

1. Introduction

While investigations of rain events are numerous (Goddard et al. 1982; Ulbrich 1983; Tokay and Short 1996; Atlas et al. 1999; Schuur et al. 2001; Zhang et al. 2001, 2003, 2006, 2008; Bringi et al. 2003; Brandes et al. 2004a,b; Thurai et al. 2007, 2014; Cao et al. 2008; Niu et al. 2010; Tao et al. 2010; Islam et al. 2012; Williams et al. 2014; Bukovčić et al. 2015), winter precipitation has been studied considerably less, especially transitions between the liquid and snow/ice phases (Raga et al. 1991;

Trapp et al. 2001; Cortinas et al. 2004; Ikeda et al. 2005a,b; Yuter et al. 2006, 2008; Brandes et al. 2007; Ryzhkov et al. 2008; Zhang et al. 2011).

Even though ice pellets (IPs) are considered to be less hazardous than snow or freezing rain, they are very important. Relatively small changes in environmental conditions can dramatically alter precipitation type from ice pellets to freezing rain or snow (Ryzhkov et al. 2011b). In recent years, there has been an increase in interest regarding the characteristics and microphysical properties of ice pellets. Gibson and Stewart (2007) used a high-resolution digital camera to photograph and classify IPs into several categories during a winter storm in Mirabel, Quebec, Canada: bulged particles, particles

Corresponding author e-mail: Petar Bukovčić, petar.bukovcic@ou.edu

with spicules, spherical particles, nearly spherical particles, and irregular particles. Gibson et al. (2009) investigated the microphysical and statistical properties of ice pellets in the Montreal, Quebec, Canada, area using the images from a high-resolution digital camera. Kumjian and Schenkman (2014) presented an analysis of a curious case of ice pellets over central Tennessee. Despite the fact that the surface temperatures were >10°C, and the lowest ~2 km of the atmosphere were entirely above freezing, ice pellets were reported on the ground. They found that the evaporation of raindrops substantially cooled the surrounding air toward its wet-bulb temperature T_w, well below 0°C. This was sufficiently cold for the freezing of subsequent raindrops, which fell to the ground without significant melting or sublimation. Nagumo and Fujiyoshi (2015) investigated microphysical properties of slow-falling and fast-falling ice pellets using 2DVD. They associated slow-falling IPs with uniform and rapid freezing in the cold and dry layer with $T_w \sim -4$°C. The fast-falling IPs showed a similarity to the ice particles with a smooth wet surface and exhibited falling velocities close to those of raindrops. Hence, fast-falling ice pellets froze slowly through contact with splinters (or ice crystals) generated by preceding slow-falling ice pellets in a relatively warm layer.

Ryzhkov et al. (2011b) and Kumjian et al. (2013) are two studies that are closely related to our research. Ryzhkov et al. (2011b) investigated polarimetric radar signatures in winter storms and their relation to aircraft icing and freezing rain; it is rather difficult to predict or even detect the transition between very disruptive freezing rain and much less hazardous ice pellets. One of the main conclusions of the study is that in the case of refreezing (i.e., IP formation), differential reflectivity Z_{DR} is locally increasing rather than decreasing, which is the opposite of what was initially expected; horizontal reflectivity Z_H and copolar correlation coefficient ρ_{hv} locally decrease in transition from rain to ice pellets (Z_H because of the change in the complex dielectric factor and ρ_{hv} because of differences in particle shapes, compositions, and canting angles at refreezing levels). Kumjian et al. (2013) conducted a study of polarimetric radar measurement fingerprints in winter storms that produce ice pellets. These unique refreezing fingerprints, observed within the low-level subfreezing layer, consist of enhancement in Z_{DR} and specific differential phase K_{DP} and decrease in Z_H and ρ_{hv}. They proposed that the unique polarimetric signature of refreezing is caused either by preferential freezing of small drops or local ice generation and suggested that the validity of these hypotheses be further explored.

The shapes in the PPI plots of the reported refreezing signatures by Ryzhkov et al. (2011b) and Kumjian et al. (2013) are rings of change in polarimetric variables below the melting layer and centered on the radar. Such rings close to the radar are readily identified at high-elevation scans because of enhanced vertical resolution and continuity in azimuth. Thus, the signatures are well suited for discrimination between freezing rain and ice pellets in operational environments. Herein, we report the polarimetric observation of ice pellets in a localized area about 30–40 km away from the radar where poorer resolution and small spatial extent challenge identification and interpretation. However, benefiting from the previous observations, a collocated 2DVD, and other measurements, we are able not only to confirm the signatures but also to quantify the amount of frozen precipitation.

In this study, we jointly use polarimetric radar data and 2DVD measurements to uncover important precipitation microphysics properties in the transitions from rain to ice pellets and vice versa. A novel way of presenting polarimetric data in quasi-vertical profiles (QVPs) from azimuthal averages (Ryzhkov et al. 2016) is expanded to generate slanted vertical profiles (SVPs), which help to understand the transition precipitation microphysics. Also, the discrepancies between radar-retrieved microphysical parameters and those obtained from 2DVD measurements are interpreted.

In section 2, the data acquisition, processing, and synoptic setting are explained; in section 3, the methodology and theoretical basis are presented. The main results of the study, as well as comparisons with the findings of Ryzhkov et al. (2011b) and Kumjian et al. (2013), are in section 4. The discussion and implications of our findings are in section 5, and the summary is in section 6.

2. Dataset and synoptic setting

Observation data of a winter storm event on 20 January 2007 were collected with the S-band polarimetric KOUN radar and the University of Oklahoma (OU) 2DVD in central Oklahoma. The case is classified as a wintery mix of ice pellet, freezing rain, and rain periods. The disdrometer was deployed at Kessler Atmospheric and Ecological Field Station (KAEFS), an OU test site approximately 29 km and 191.4° azimuth from KOUN, at ~345 m MSL. Disdrometer-measured drop size distributions (DSDs; for raindrops) or particle size distributions (PSDs; for hydrometeors other than rain) are sampled over 1-min intervals.

On this day, an upper-level, low pressure system approached the area from the southwest, passing to the northeast. The event started at about 0540 UTC with light stratiform rain over the disdrometer site, changing into periods of IPs approximately from 0645 to 1100 UTC and approximately from 1730 to 2130 UTC, called the primary and secondary ice pellet periods (see section 4b for detailed analysis). In general, the transition was caused by a warm layer of air at ~2200 m above the ground and a freezing layer below the warm layer extending to the ground, making environmental conditions favorable for ice pellet formation; the structure of the melting–refreezing layers is more complex and described in section 4a. Precipitation was mainly freezing rain or rain with a few short transitions to ice–mixed phase between the primary and secondary ice pellet periods. Near the end of the event, from 2200 until 2330 UTC, precipitation changed from IP–mixed phase to snow.

3. Methodology

The fundamental information associated with rain microphysics is contained in raindrop size distributions. DSDs are readily measured with 2DVDs, but only at one location. Various microphysical parameters, such as median volume diameter D_0 (mm) and rainfall rate R (mm h^{-1}), can be calculated from DSDs obtained from 2DVD measurements for a 1-min time interval:

$$\int_0^{D_0} D^3 N(D)\, dD = \int_{D_0}^{\infty} D^3 N(D)\, dD \quad \text{and} \quad (1)$$

$$R = 10\pi \sum_{i=1}^{L} \frac{C(D_i) D_i^3}{A(D_i)}. \quad (2)$$

The term $C(D_i)$ represents the number of particles, $A(D_i)$ is the mean measured sensor (2DVD) effective area in millimeters squared for the size bin i, and D_i is the equivolume diameter representing the bin center (also denoted as D subsequently) in millimeters, while $N(D)$ is measured drop size distribution (m^{-3} mm^{-1}). If the ice phase is assumed instead of liquid precipitation, the rainfall rate becomes the ice pellet equivalent liquid fall rate R_{ip} (mm h^{-1}) for a 1-min summation interval:

$$R_{ip} = 10\pi \frac{\rho_{ice}}{\rho_w} \sum_{i=1}^{L} \frac{C(D_i) D_i^3}{A(D_i)}, \quad (3)$$

where $\rho_{ice} = 0.917$ g cm^{-3} is the density of ice and ρ_w is the density of water.

Integral parameters calculated from 2DVD measurements for liquid precipitation, reflectivity factor

$[Z_{h,v}$ (mm^6 m^{-1}) and $Z_{H,V}$ (dBZ); Doviak and Zrnić 1993], differential reflectivity Z_{DR} (dB), and copolar correlation coefficient ρ_{hv} are defined as

$$Z_{h,v} = \frac{4\lambda^4}{\pi^4 |K_W|^2} \int_{D_{min}}^{D_{max}} |s_{h,v}(\pi, D)|^2 N(D)\, dD, \quad (4)$$

$$Z_{H,V} = 10 \log_{10}(Z_{h,v}), \quad (5)$$

$$Z_{DR} = 10 \log_{10}(Z_h / Z_v), \quad \text{and} \quad (6)$$

$$\rho_{hv} = \frac{\left| \int_{D_{min}}^{D_{max}} s_v(\pi, D) s_h^*(\pi, D) N(D)\, dD \right|}{\sqrt{\int_{D_{min}}^{D_{max}} |s_v(\pi, D)|^2 N(D)\, dD \int_{D_{min}}^{D_{max}} |s_h(\pi, D)|^2 N(D)\, dD}}. \quad (7)$$

Backscattering amplitudes obtained from T-matrix calculations are represented by $s_{h,v}(\pi, D)$; the conjugate is indicated by *, and indices h and v denote horizontal and vertical polarization. Scattering amplitudes of ice pellets are calculated using Rayleigh–Gans approximation where the dry graupel–hail axis aspect ratio (Ryzhkov et al. 2011a) is

$$r_{dh} = 1 - 0.02D. \quad (8)$$

In the case of raindrops, the axis ratio (Brandes et al. 2002; Zhang 2016)

$$r_w = 0.9951 + 0.0251D - 0.036\,44D^2 + 0.005\,303D^3 - 0.000\,249\,2D^4 \quad (9)$$

is assumed for retrievals and comparisons.

Polarimetric radar data can be utilized to determine the particle size distribution of the hydrometeors (Zhang et al. 2001). The gamma distribution

$$N(D) = N_0 D^\mu \exp(-\Lambda D) \quad (10)$$

has been widely accepted to model rain DSDs (Ulbrich 1983). The N_0 (mm$^{-1-\mu}$ m^{-3}) is the number concentration parameter, μ is the distribution shape parameter, and Λ (mm^{-1}) is the slope parameter. The following constraining relation (Cao et al. 2008), empirically derived from 2DVD measurements of rain in Oklahoma, is used for rain microphysical retrievals in this study:

$$\mu = -0.0201\Lambda^2 + 0.902\Lambda - 1.718. \quad (11)$$

The μ–Λ relation used for the ice phase precipitation (ice pellets),

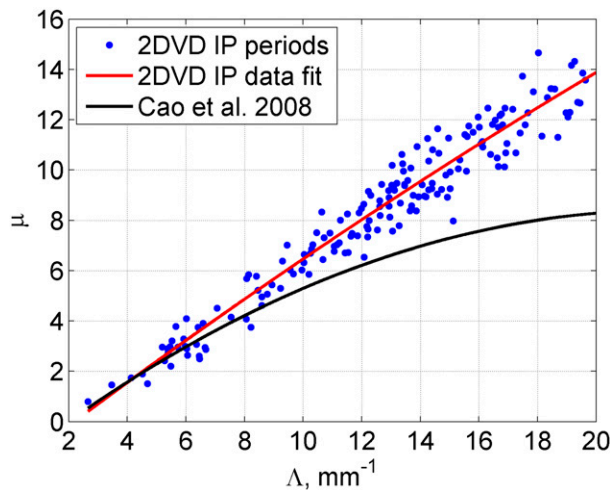$$\mu_{ip} = -0.0048\Lambda^2 + 0.8856\Lambda - 1.9124, \quad (12)$$

FIG. 1. A μ–Λ scatterplot where the blue dots are estimated values of μ and Λ from 2DVD measurements using the second, fourth, and sixth moments of the measured distributions during the IP periods (0645–1100 UTC and 1730–2130 UTC). The red line denotes the second-degree polynomial data fit during these periods, and the black line represents the rain μ–Λ relation from Cao et al. (2008).

is derived from periods identified as IP and measured with 2DVD. This μ–Λ relation (Fig. 1) is obtained from the second, fourth, and sixth moments of the measured PSDs.

Parameters N_0 and Λ of the constrained [via Eqs. (11) and (12)] gamma distribution are directly estimated from radar measurements of Z_H and Z_{DR}, respectively, as explained in Zhang (2016). From this distribution, various precipitation parameters, such as median volume diameter D_{0r}, rainfall rate R_r, and ice pellet liquid water equivalent rate R_{ipr}, are retrieved:

$$\int_{D_{min}}^{D_{0r}} D^3 N(D)\, dD = \int_{D_{0r}}^{D_{max}} D^3 N(D)\, dD, \qquad (13)$$

$$R_r = 6 \times 10^{-4} \pi \sum_{i=1}^{L} D_i^3 v(D_i) N(D_i) \Delta D, \quad \text{and} \quad (14)$$

$$R_{ipr} = 6 \times 10^{-4} \pi \frac{\rho_{ice}}{\rho_w} \sum_{i=1}^{L} D_i^3 v(D_i) N(D_i) \Delta D. \quad (15)$$

The quantities D_{min} and D_{max} are particles' minimum (set to 0.1 mm) and maximum diameters, where D_{max} can be estimated from the radar reflectivity (or differential reflectivity; Brandes et al. 2003); $v(D_i)$ denotes the raindrops' terminal velocity in meters per second (Brandes et al. 2002), and the same is used for the IP terminal velocity as suggested by 2DVD measurements (see section 4b for clarification). The ΔD is bin spacing, set to 0.2 mm in our computations.

To interpret radar measurements over the disdrometer site, we use representations in the vertical
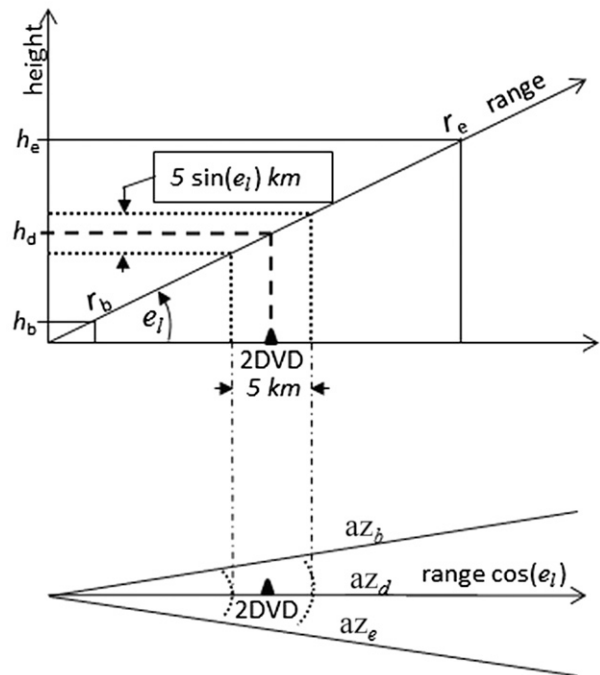

FIG. 2. Diagram explaining computation of the SVP and its interpretation. For simplicity, a flat Earth is assumed in the sketch, whereas in actual computations, Earth's curvature is accounted for via the 4/3 equivalent radius model. The vertical plane bisects the radar and disdrometer locations. The projection of the conical section over which the data are averaged is at the bottom of the figure. The disdrometer is located at 29 km from the radar; the extent of averaging in azimuth $az_e - az_b = 20°$. In the data interpretation, the band of values $5 \sin(e_l)$ km wide and centered at the height above the disdrometer is examined.

planes. Herein, two such representations are explained. The first, SVP, was inspired by the QVP introduced by Ryzhkov et al. (2016) to analyze vertical structure at a higher resolution. Our SVP profile is presented in the vertical cross section positioned along the radial that is located over the disdrometer. Figure 2 illustrates how one vertical profile along height is obtained. The radial over the disdrometer (2DVD) has azimuth az_d and elevation e_l, which in our case is $\leq 1°$. A beginning range r_b and ending range r_e are chosen so that the disdrometer is about at the midpoint. Similarly, a beginning azimuth az_b and ending azimuth az_e are chosen to encompass the disdrometer's azimuth. Data from radials at adjacent azimuths between az_b and az_e, same e_l, and constant range are averaged to produce a single value. The array of such points along range is the radial profile of the variable. Then the data from r_b to r_e are projected on the vertical axis to produce an SVP corresponding to the time of the scan. Typically, the range interval is up to 60 km and the azimuthal span is 20°. *The data over such large-range intervals are likely inhomogeneous; hence,*

interpretation needs to be very cautious. Clearly, relating the top of the profile to the bottom could produce absurd results. But in our interpretation, we do not attempt to relate data from vastly different ranges. Rather, we concentrate on the height h_d, which is directly over the disdrometer site. Then we examine a small increment above and below this height to interpret the change in the polarimetric variables. The small increment corresponds to the range interval of 2.5 km, for a total of 5 km centered on the disdrometer, making the vertical extent equal to $5\sin(e_l)$ km (Fig. 2). Over such short range, the homogeneity is much more likely to hold, although it is not guaranteed. An additional concern is smoothing by the beam, which, at the disdrometer site, extends over about 500 m. The beam positions in the SVP are such that the edge (3 dB point) of the beam does not reach the bright band. Hence, the data are not contaminated by the strong gradient of Z_H at the transition from the bright band to the precipitation below. At the disdrometer location, the azimuthal averaging sector equals 10 km. Note that in our analysis, Earth's curvature and the 4/3 radius model are taken into account but are not presented in the simplified diagram (Fig. 2).

The second presentation in the vertical plane we call enhanced vertical profile (EVP). This profile is constructed from all available elevation scans over the disdrometer. At each elevation, a median is applied to three radials and five range locations starting 2.5 km before the disdrometer. The procedure is repeated in the range up to 2.5 km beyond the disdrometer location. These median values are projected from all elevations to the vertical to create one vertical cut (EVP) over the disdrometer (see Fig. 7).

An additional presentation convenient for a time series of variables uses only the median of the three (in azimuth) by five (in range) points above the disdrometer at a fixed elevation. Herein, this is applied to data at the two lowest elevations (see Figs. 11 and 12).

The identification of the precipitation phase change in the 2DVD data was accomplished by a visual examination of the images, which exhibit a clear distinction between irregular shapes of ice hydrometeors and oblate raindrops (some images are in Fig. 4).

4. Results

The principal findings of the study are in this section, which consists of five subsections corresponding to the five topics as follows: environmental data, 2DVD data, radar data, refreezing model, and radar–2DVD comparisons.

a. Environmental data

In the preliminary data perusal, the vertical profiles from the radiosondes (available

at http://weather.uwyo.edu/upperair/sounding.html) and Rapid Update Cycle (RUC) analysis (available at http://nomads.ncdc.noaa.gov/data/rucanl/200701/20070120/) were examined, as presented in Figs. 3a–c for 0000, 1200, and 1800 UTC, respectively, for the Norman, Oklahoma, radar (KOUN) location. Generally, these are well matched (especially temperature), with minor discrepancies in dewpoint temperature, which are mostly in drier air where the RUC slightly overestimates dewpoint temperature (Fig. 3a). Some subtle differences (up to a few degrees Celsius) also exist between radiosonde and RUC temperature profiles when multiple melting and freezing layers are present (Fig. 3a). Because the temporal resolution of the radiosondes' measurements is very sparse and available only at 6-h intervals, RUC analysis soundings are examined for better insight into environmental conditions. The time evolution of RUC analysis temperature and relative humidity vertical profiles over the 2DVD location (KAEFS) are plotted in Figs. 3d,e. RUC temperature profiles are compared with radio acoustic sounding system (RASS) profiles (Fig. 3f) obtained from the collocated NOAA's Purcell, Oklahoma, wind profiler. The RASS measurements could only be obtained in conditions of little to no precipitation; thus, no reliable data are recorded after ~1130 UTC. Nonetheless, RUC analysis temperature profiles match well with RASS measurements between 0100 and 0400 UTC, where the temperatures above 0°C extend from ~2500 m MSL to the ground, with the elevated freezing layer centered at ~1500 m approximately between 0200 and 0300 UTC. As seen in earlier comparisons between RUC and radiosonde profiles (e.g., 0000 UTC for the Norman OUN location; Fig. 3a), RUC does not reproduce the elevated melting layer approximately from 2200 to 3000 m MSL at 0000 UTC, which clearly exists in the RASS profile. Also, there is no indication of a melting layer above the ground in the RUC profile between 0800 and 1130 UTC, but a melting layer is seen in the RASS data at ~2000 m MSL until ~1000 UTC, when the RASS measurement started to become unreliable. There is presence of a freezing layer in the RASS data approximately from 0700 until 1130 UTC, extending approximately from 700 to 1700 m MSL, which is also present in the RUC profile with minimum temperatures from both sources close to −3°C. The air is relatively dry (from 0000 until 0930 UTC) in the layer extending from ~3000 m to the ground, as seen in the RUC relative humidity profile (Fig. 3e). There is also a nearly saturated layer (>95% RH) aloft at ~3000–5000 m MSL for the same period. Air becomes nearly saturated from 1200 UTC until the end of the event at low- and midtropospheric levels (0–5000 m MSL).

In summary, all available data sources (including the KOUN radar) show that the temperature profile
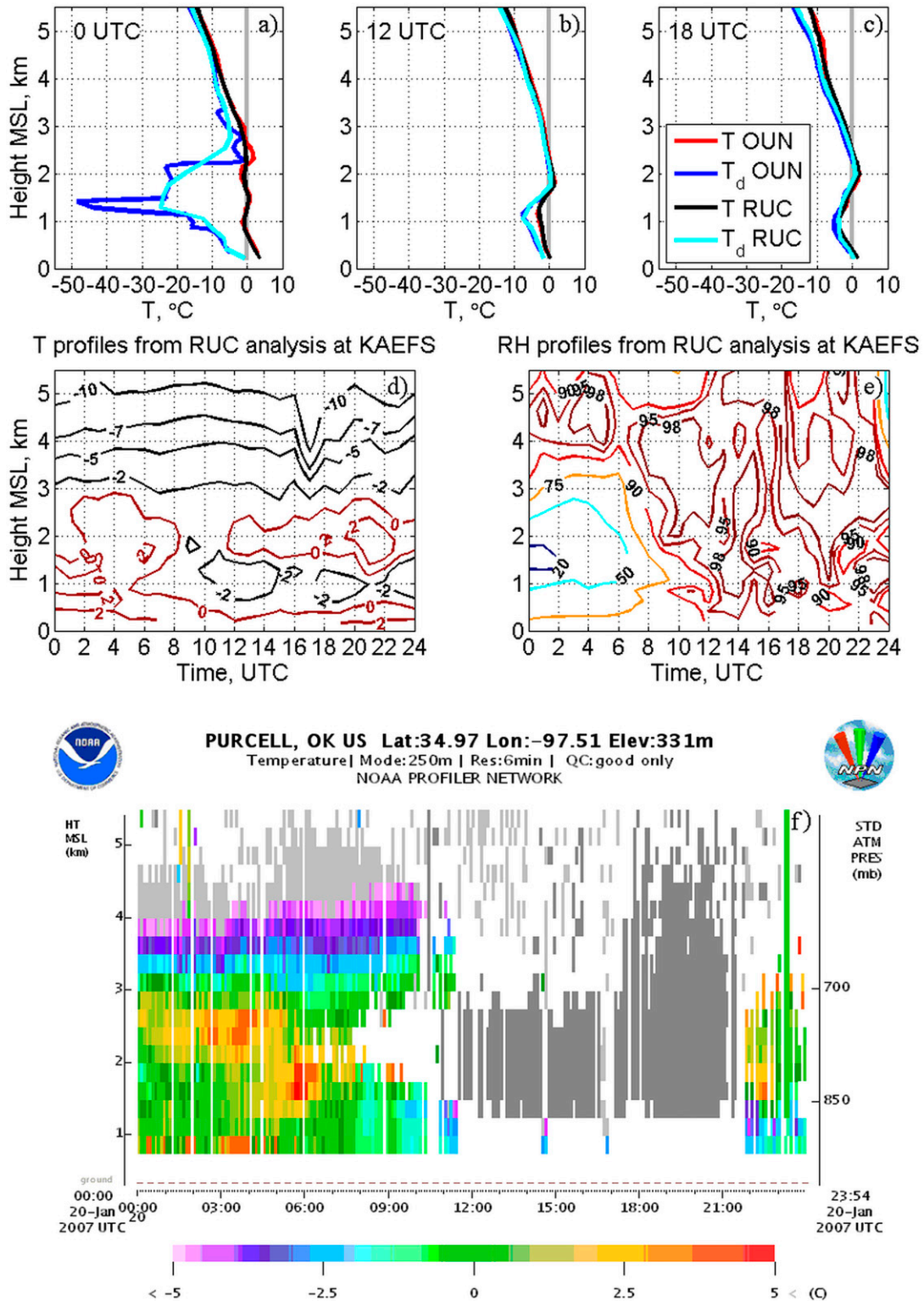
FIG. 3. Comparison of radiosondes and RUC analysis soundings for Norman (KOUN) at (a) 0000, (b) 1200, and (c) 1800 UTC. Evolution of (d) temperature and (e) relative humidity profiles over KAEFS. (f) Temperature profiles from the RASS soundings Purcell profiler at KAEFS.
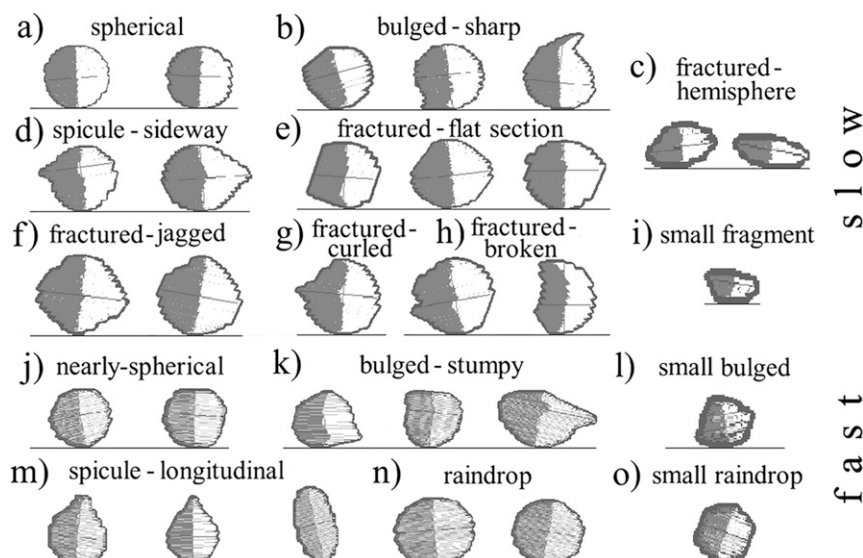
FIG. 4. Images of IPs and raindrops from 2DVD (not to scale); shown are typical silhouettes of (a)–(i) slow-falling IPs, (j)–(m) fast-falling IPs, and (n)–(o) raindrops. The particles in (c), (i), (l), and (o) ≤ 1 mm, whereas the other particles' dimensions are between 1.5 and about 3 mm. The fast particles' fall speeds are about the same as those of raindrops. The slow particles' fall speeds were between 55% and 80% smaller than those of equivalent-size raindrops.

exhibited very complex multiple melting–refreezing layered structures. At the beginning of the event, the double melting and refreezing layers are suggested by the inferred temperature profile. The primary melting layer [~700–2000 m above ground level (AGL)] is accompanied by the shallow refreezing layer and a secondary shallow melting layer toward the ground. Surface temperature suggests a secondary shallow refreezing layer next to the ground. This complex structure gradually evolved to a stronger melting layer aloft, with increased height and depth (from 1230 to 2100 UTC), and refreezing occurred at lower altitudes than in previous stages.

b. Data from the 2DVD

The images and velocities of particles measured by the 2DVD are analyzed next. A high percentage of recorded ice pellets (>99%) exhibited fast-falling velocities, very close to those of raindrops; hence, it was difficult to distinguish between the precipitation types using measured velocity distribution. In contrast, only a few IPs displayed slow-falling velocities ranging over 1–3 m s^{-1}. In a study by Nagumo and Fujiyoshi (2015), the number of fast-falling ice pellets was higher than the number of slow-falling ice pellets but comparable (for IPs >1.5 mm in diameter, the ratio was roughly 3:1 in favor of fast falling). In our study, slow-falling IPs were identified with 2DVD by looking into both falling velocities and images from orthogonal cameras, whereas fast-falling

IPs were identified visually. Images of both fast and slow IPs recorded with the 2DVD are in Fig. 4. In general, larger IPs ($D > 1.5$ mm) are easily identified because of rugged shapes that deviate from the oblate shapes of the same-sized raindrops (Fig. 4). Smaller IPs ($D < 1$ mm), especially near spherical, are much harder to discriminate from the similar-sized raindrops because of the 2DVD's resolution (~0.2 mm in horizontal) and because of the particle's contour depiction by the 2DVD visualization software (as seen in Fig. 4). Therefore, we assume that if larger particles are identified as rain, smaller ones in the same period are assigned to the rain category, although some could be partially frozen. If the larger particles are ice pellets, then the smaller ones must be pellets too, as these would have frozen before the larger ones.

The disdrometer measurements suggest that the primary ice phase period occurred between 0645 and 1100 UTC, and a secondary period was approximately from 1730 to 2130 UTC. Between 1100 and ~1730 UTC, freezing rain and rain are the dominant types of precipitation, with just a few shorter ice phase transitions until 2130 UTC, when precipitation started changing into snow (not shown). Temperature measurements from the nearby Washington, Oklahoma, mesonet station (not shown) indicate that freezing at 1.5 m above ground level occurred approximately from 0720 to 1430 UTC, partially coinciding with the primary ice pellet periods. The lowest temperature was about −0.5°C from
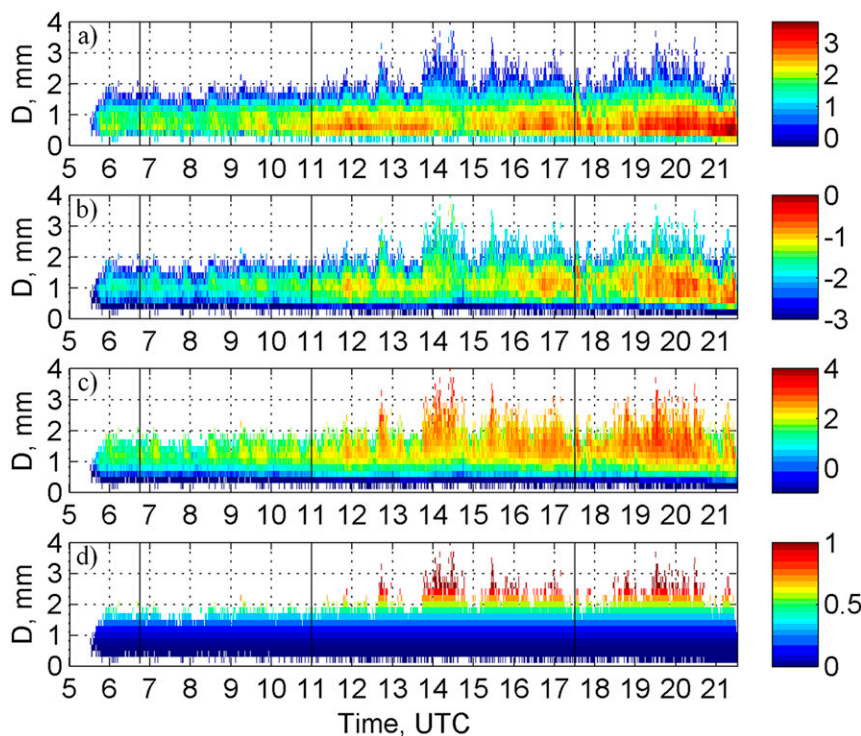
FIG. 5. Evolution of (a) DSD $[\log_{10}(\text{m}^{-3}\,\text{mm}^{-1})]$, (b) mass $[\log_{10}(\text{g}\,\text{m}^{-3}\,\text{mm}^{-1})]$, (c) Z_H $[\log_{10}(\text{mm}^6\,\text{m}^{-3}\,\text{mm}^{-1})]$, and (d) Z_{DR} (dB) distributions measured with 2DVD; thin black lines denote main IP periods approximately from 0645 until 1100 UTC and 1730 to 2130 UTC.

1030 until 1200 UTC. The temperature at 9 m above ground level implies that freezing occurred from 0615 until 2130 UTC, with the lowest temperature of about $-0.8°$C from 1100 until 1215 UTC.

The time evolutions of the DSD, mass, Z_H, and Z_{DR} distributions measured–calculated from the 2DVD are shown in Figs. 5a–d, where Z_H and Z_{DR} are obtained from the measured DSDs assuming liquid phase. The mass was computed for each size bin assuming liquid density and the volume of the particle at the observed equivalent diameter D_i. The simulated radar variables were similarly computed at each size category using the T matrix and relations between the size and the variable in the case of the liquid phase. The results are plotted as a distribution with respect to D_i.

In the primary ice pellet period (from approximately 0645 until 1100 UTC, denoted by thin vertical black lines), DSD values are smaller than in the rain periods and range up to $\sim$240 m^{-3} mm^{-1} (at $\sim$0.6-mm size). The DSDs are initially narrow (before 1030 UTC) and gradually broaden with time in the mature stage, which predominantly consists of rain periods. In the secondary IP period (1730–2130 UTC, denoted by a thin vertical line), there are several periods of IPs alternating with rain/freezing rain. In comparison with earlier storm

stages, DSD values are larger, and the highest concentrations coincide with the occurrence of rain. In general, larger concentrations of particles are seen from 1100 to 2130 UTC for diameters D = 0.4–1.6 mm, with the highest value at about 2120 UTC with $N(D)$ of approximately 4500 m^{-3} mm^{-1} for D of approximately 0.7 mm. Particles with sizes between 0.9 and 1.3 mm contribute to the maxima in the mass distribution, while larger drops contribute the most to the maxima in reflectivity and differential reflectivity distributions.

c. Radar data

The morphology of the storm is observed in the fields of Z_H, Z_{DR}, and ρ_{hv} (Figs. 6a–c; 0730 UTC) displayed on conical surfaces (PPI). The Z_H varied between 0 and 20 dBZ in the beginning of the event, whereas in later stages of the storm, it increased up to $\sim$40 dBZ. The Z_{DR} values were noisy most of the time but generally did not exceed 2 dB, not even in the middle stages when rain was a dominant type of precipitation. At $\sim$0730 UTC (Figs. 6a–c), there is a localized drop in Z_H and ρ_{hv}, coinciding with the measurable enhancement of Z_{DR} in the vicinity and southwest of the 2DVD location, marked by magenta times signs in Figs. 6a–c. The 2DVD indicates ice pellets at this time. Thus, we attribute the described
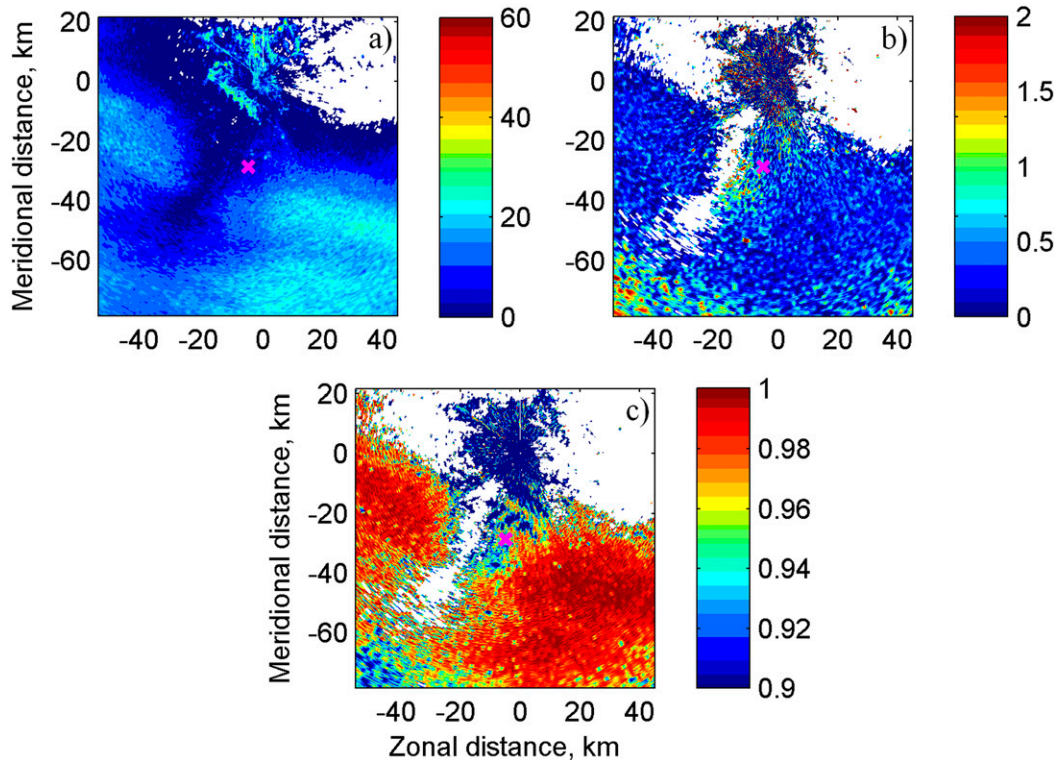
FIG. 6. PPI of (a) Z_H, (b) Z_{DR}, and (c) ρ_{hv} at 0730 UTC and an elevation of 0.41°. The magenta times signs represent the 2DVD location (KAEFS). The high values of Z_H extending diagonally from NW to SE at about 10 km off the radar are an orographic ridge, which, in this case, shields the disdrometer location from the influence of ground clutter.

change of the polarimetric variables to refreezing associated with the ice pellets. The "refreezing patch" disappeared later during the rain period, suggesting that the phenomenon is real. Ryzhkov et al. (2011b) and Kumjian et al. (2013) reported a repetitive ringlike structure of enhanced Z_{DR} and reduced ρ_{hv} values (reduction in Z_H occurs as well but gradually along the radial instead of in a localized ring) in PPIs at intermediate or higher elevations (>3°) if refreezing is ongoing. Their cases were more spatially uniform, and refreezing was widespread across radar coverage area, thus much easier to interpret. This contrasts the patchy and very localized occurrence about 30–40 km south-southwest from the radar in our case. Also, the height of the refreezing layer in our case is lower: it ranges from ~70 to ~700 m AGL, as compared with from ~400 to ~800 m in Ryzhkov et al. (2011b), or from ~300 to ~1000 m in Kumjian et al. (2013). Another very important difference is that the minimum temperature of the refreezing layer, or "refreezing zone" as dubbed in Ryzhkov et al. (2011b), in our case rarely dropped below −4°C (from Norman radiosonde soundings at 1200 and 1800 UTC, RASS, and RUC temperature profiles), whereas it ranged from −5° to −12°C in these previous studies.

The time evolution of the enhanced vertical profiles (EVPs are explained in section 3) of the radar variables Z_H, Z_{DR}, and ρ_{hv}, created from volume PPI scans over the disdrometer site, are presented in Figs. 7a–c; overlaid are RUC temperature vertical profiles (black dashed lines represent below freezing temperatures, and magenta dashed lines represent above freezing temperatures). In all three polarimetric variables, the melting layer is well defined with the increased Z_H and Z_{DR} but reduced ρ_{hv} values. The height of the melting layer from RUC analysis soundings agrees well with that seen in the polarimetric measurements (~2 km AGL) except from ~0800 until 1130 UTC, when RUC soundings show only freezing temperatures (although relatively close to 0°C), as described earlier (Fig. 3d). The evolution of Z_H, Z_{DR}, and ρ_{hv} (Figs. 7a–c) reveals the presence of a weaker melting layer centered at ~1900 m AGL (approximately 2250 m MSL) from ~0800 until 1130 UTC. Over the primary period of ice pellets (0645–1100 UTC), Z_H values are very low (0–10 dBZ) within the sublayer from ~700 m extending close to the ground. The trend of lower values of Z_{DR} (from 0 to 0.5 dB) and ρ_{hv} (0.9–0.95) within the sublayer is also seen. Low Z_H and Z_{DR} could be due to either
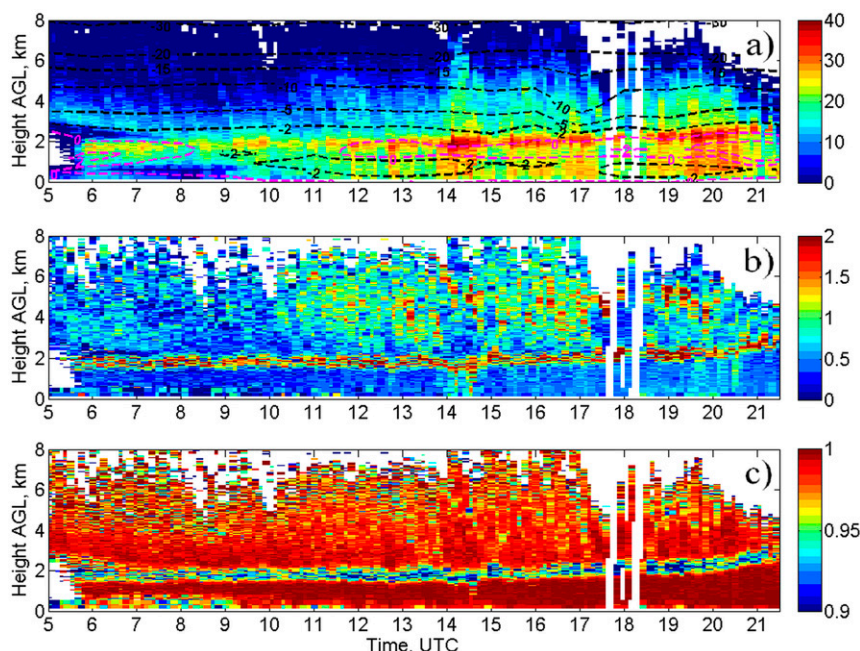
FIG. 7. Evolution of EVPs of (a) Z_H, (b) Z_{DR}, and (c) ρ_{hv} measured by KOUN over the 2DVD site. Height is referenced AGL. Dashed lines denote RUC analysis temperature profiles above the 2DVD location, where black represents temperature below freezing and magenta represents above freezing.

small raindrops ($D < 1.5\,mm$) or ice pellets. Although the reductions in Z_H and ρ_{hv} within the sublayer are obvious throughout the period of interest, the localized coinciding increase in Z_{DR} is not. There are some hints of about 0.2 to 0.3 dB increase in Z_{DR} next to the ground. On the onset of precipitation, at about ~0545 UTC, there is a short period of warming, as both RASS and RUC indicate (at ~1500 m MSL), coinciding with the temporary strengthening of the bright band, followed by the slightly enhanced values of the Z_H extending all the way to the ground. During the primary ice pellet period, the bright band is weaker than during the later periods of rain, and the melting layer is shallower, with the refreezing layer temperature estimated from RASS and RUC profiles to be no lower than −3.5°C. In general, moisture availability gradually improves from the onset of precipitation at ~0545 UTC throughout the event (in the lowest 3000 m), modifying the air from unsaturated to slightly subsaturated with respect to water and (most likely) saturated with respect to ice (Fig. 3e). All of these environmental conditions made the period approximately from 0645 to 1100 UTC favorable for ice pellet formation. During the secondary IP period, there are also hints of refreezing signatures in EVPs between 1815 and 2015 UTC (lowest 300 m) but slightly weaker than during the previous IP period because refreezing occurred at even lower altitudes. This is partially caused by

the increased height and depth of the melting layer, allowing particles to almost entirely melt, thus needing more time to refreeze. From 1730 until ~2200 UTC, the lower-tropospheric levels (1–1.5 km) become more suitable for evaporative cooling to occur, resulting in frequent IP appearances during the period.

Our 2DVD location is approximately 29 km south from the radar, and coincidently favorable conditions for the ice phase precipitation are found close to the disdrometer site. Moreover, refreezing was localized at lower altitudes (from ~70 to ~700 m AGL). This motivated construction of SVPs (defined in section 3) at the lowest elevations. The SVP at 1° elevation (Fig. 8 within the box) between 0645 and 0915 UTC clearly displays the onset of the refreezing signature. The box isolates parts of the refreezing layer approximately from 550 to 660 m AGL. The Z_H and ρ_{hv} decrease (Z_H about 5–7 dB and ρ_{hv} of approximately 0.02) toward the ground, while the Z_{DR} has a weak local maximum (~0.4–0.6 dB). Similarly, the SVP reconstructed from the 0° elevation (Fig. 9) indicates a refreezing layer (times 0645–1100 UTC and height 90–110 m AGL). Further examination of the data, including temperature (Fig. 7), suggests that partial melting could have occurred above 110 m. We speculate that the Z_H in Fig. 9 is higher than in Fig. 8 because of this partial melting. Two warm layers with a cold layer in between them are clearly seen in Fig. 7.
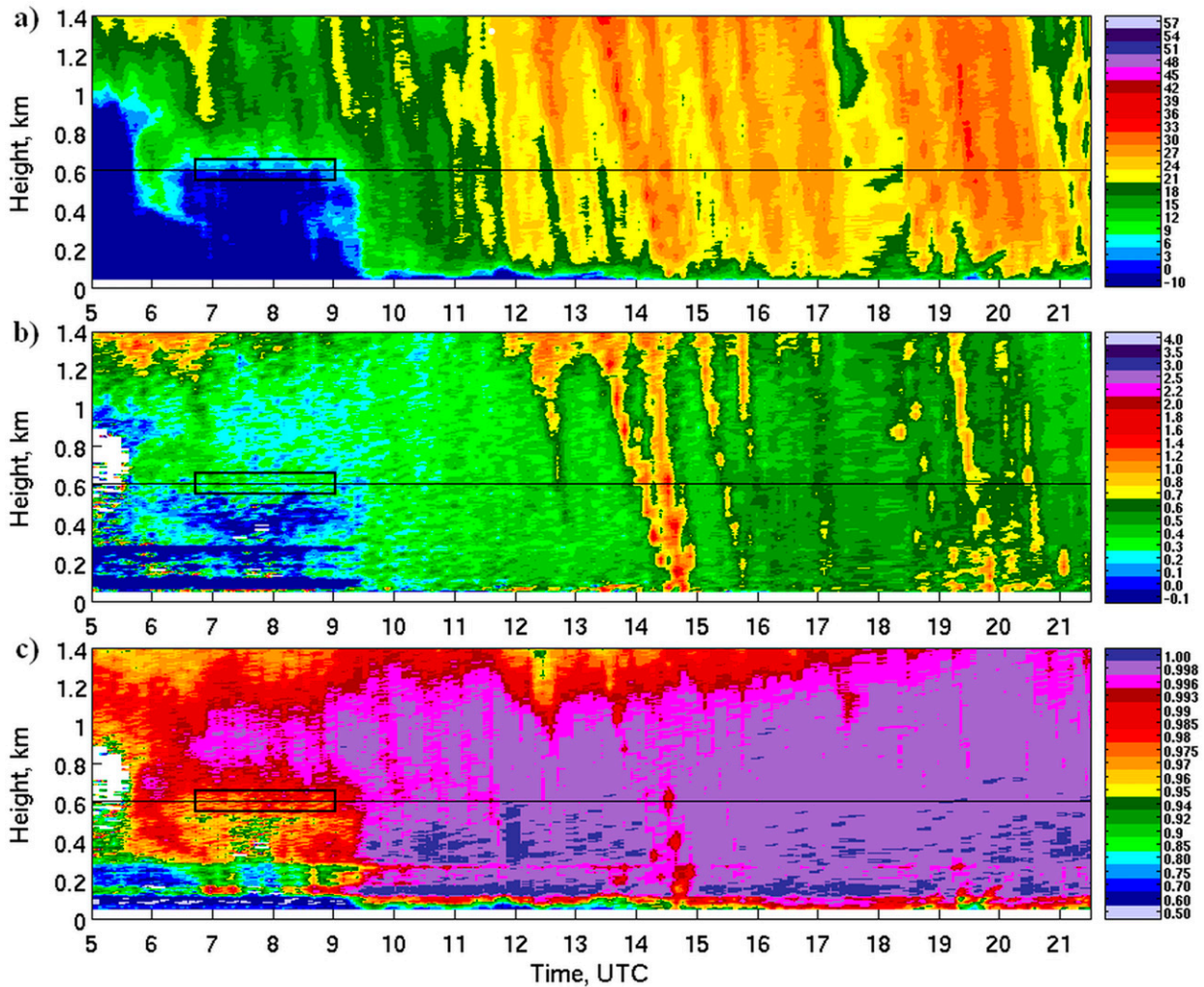
FIG. 8. Evolution of SVPs at 1° elevation of (a) Z_H, (b) Z_{DR}, and (c) ρ_{hv} from KOUN. The thin black horizontal lines at ~610 m AGL represent the height directly above 2DVD location; the thick black boxes represent 5-km radial segments along the 1° elevation (height projections) centered on 2DVD location and indicate a period of refreezing.

Because the temperatures at 9 m AGL were negative from 0615 until 2100 UTC and also at 1.5 m AGL from 0720 to 1430 UTC, there was an additional cold layer below the second warm layer, implying two regions of refreezing. The decrease in Z_H (4–7 dB), the persistence of Z_{DR} (0.5–0.9 dB), and local minimum of ρ_{hv} (0.92–0.95) are consistent with refreezing. The fact that this SVP projects the radial at 0° elevation (using a 4/3 Earth curvature model) makes the interpretation challenging.

The secondary IP period from 1730 to 2130 UTC, interrupted with a few short rain episodes, is identified in the disdrometer data. The refreezing periods, lasting ~20 min and centered at about 1730, 1815, 1855, 1940, 2015, 2035, and 2110 UTC, are marked by thick black boxes (Figs. 9a–c) encompassing slight enhancement in Z_{DR} (0.1–0.3 dB) and reduction in Z_H (3–6 dB) and ρ_{hv}

(by about 0.03). Radar PPI plots (not shown) indicate the freezing patch was centered west of the 2DVD, and its eastern edge was barely over it. Thus, azimuthal averaging reduced its signature in the SVP presentation. The SVP from the 0.41° (not shown), at just a bit higher altitude above the 2DVD site, exhibits one similar feature at 1815 UTC as the one from 0° elevation but not the others. This is because the refreezing patch drifted west, the melting layer intensified, and the refreezing layer lowered.

In all data, the SNR within the refreezing area is larger than 15 dB, and most values are between 20 and 30 dB. The effects of noise on the polarimetric variables were corrected to eliminate bias. Thus, the variability is caused by meteorological conditions and the statistical uncertainty, which increases at lower ρ_{hv}. Refreezing is
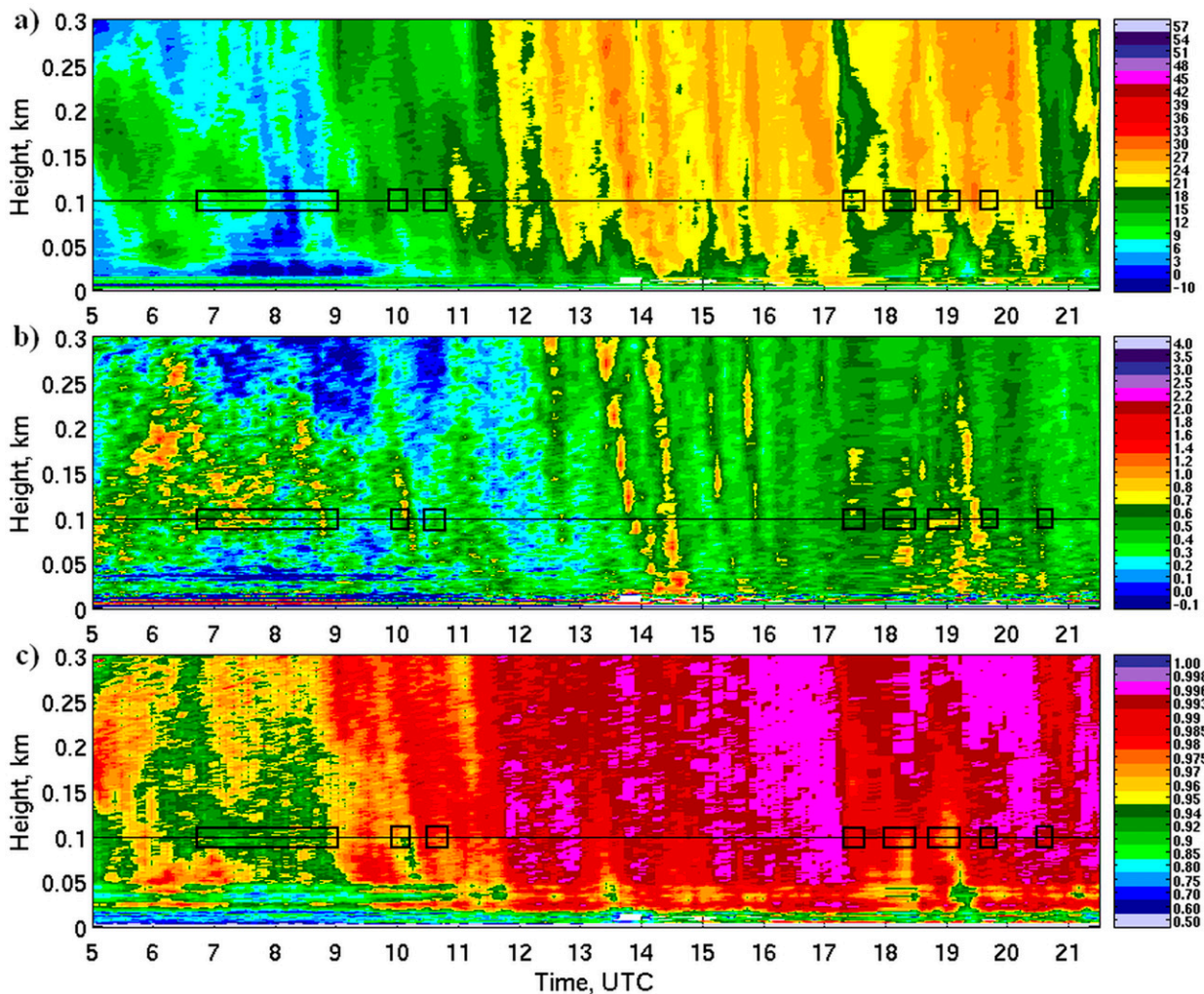
FIG. 9. As in Fig. 8, but for 0° elevation and the black lines are now at approximately 100 m AGL.

close to the ground and within a layer smaller than beam resolution, obscuring detection. A further complication is the double melting and refreezing suggested by the inferred temperature profile at the beginning of the event. Nonetheless, examination of polarimetric signatures clearly demonstrates that precipitation other than pure rain is occurring. Without the disdrometer, it would be hard to discriminate with polarimetric variables between ice pellets and slush.

d. Refreezing model

Kumjian et al. (2013) proposed two plausible mechanisms for a polarimetric refreezing signature: preferential freezing of small drops and local ice generation. In our case, local ice generation seems highly unlikely because of relatively high freezing temperatures ($>-4°C$) and weak Z_{DR} increase (pointing toward more spherical particles) in the "refreezing." Preferential freezing of

small drops gradually decreases the effects of the complex dielectric constant because of sequential freezing of, first, small drops followed by larger drops until all are frozen. The expected total decrease in Z_H is about 6–7 dB. Similar to Kumjian et al. (2013), we use the Marshall–Palmer DSD model to calculate Z_H and Z_{DR} for different rainfall rates (0.1, 0.3, 0.5, and 1 mm h^{-1}) and two size spectra, $0.05 < D < 2$ mm and $0.05 < D < 4$ mm; these maximum diameter values were observed with the 2DVD. We use 0.05-mm size increments to explore the validity of this hypothesis. Disdrometer measurements indicate that rainfall rates (or more appropriate R_{ip} rates) for the primary IP period are rather small (see Fig. 11c), less than 0.5 mm h^{-1}, hence much smaller than in Kumjian et al. (2013) simulations. In addition, 2DVD-measured drop size spectra are narrow during the primary IP period, with $D < 2$ mm. Later IP periods have slightly larger particle sizes, up to ~4 mm.
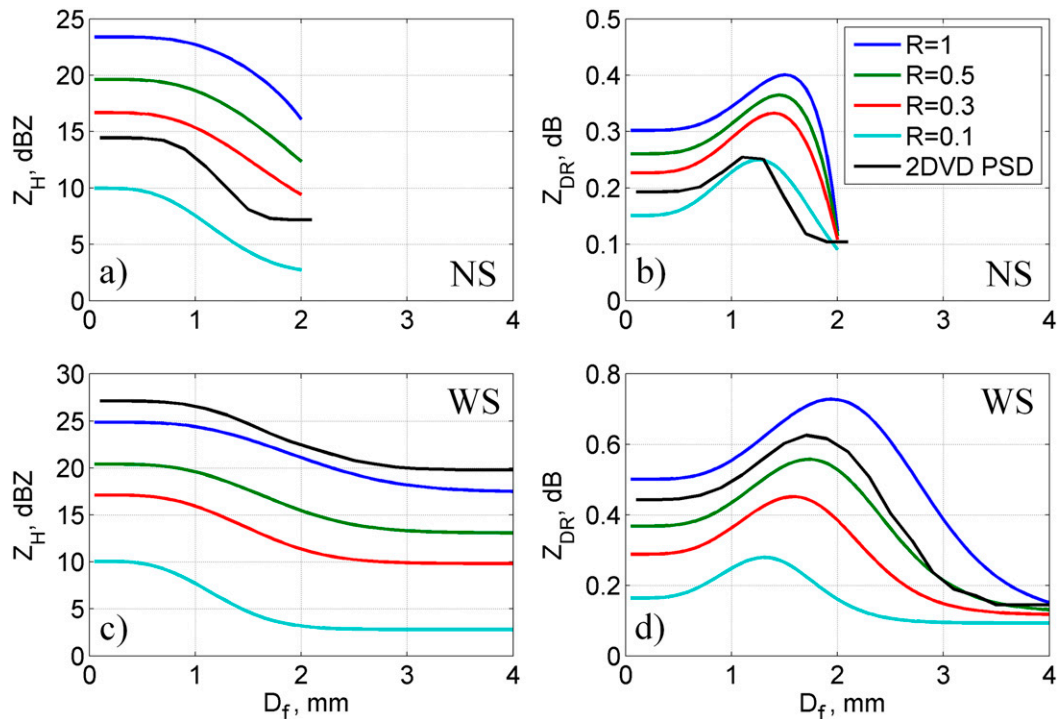
FIG. 10. The impact of drop sequential freezing for two different size spectra on (a),(c) Z_H and (b),(d) Z_{DR} for the preferential freezing of small drops. The quantity D_f is the largest frozen diameter below which all of the drops are frozen for each PSD realization. Computations are for S-band and MP DSDs with different rainfall rates R (mm h^{-1}) used (blue, green, red, and cyan represent 1, 0.5, 0.3, and 0.1 mm h^{-1}, respectively). The discretization of DSD is performed for the two spectral sizes, (top) NS and (bottom) WS, by sorting drops between 0.05 and 2 (4) mm in 40 (80) bins using 0.05-mm increments. Black lines are mean 2DVD PSD measurements from the two main IP periods: (a) and (b) are from 0645 to 1100 UTC and (c) and (d) are from 1730 to 2130 UTC.

The impact of preferential freezing of small drops for narrower spectra [narrow size (NS); 40 DSD bins, $0.05 < D < 2$ mm] on Z_H and Z_{DR} are presented in Figs. 10 a,b, while computations for broader spectra [wide size (WS); 80 bins, $0.05 < D < 4$ mm] are in Figs. 10 c,d. Preferential freezing is simulated by sequentially "freezing" each DSD diameter (bin), starting from the smallest size, where Z_H and Z_{DR} are calculated as a function of frozen diameters (D_f). Both NS and WS computations show a decrease of Z_H by ~7 dB with sequential freezing; the faster decrease of Z_H occurs for smaller sizes and NS simulation in general. The maximal Z_{DR} happens later for larger particles because of the greater relative contribution of larger liquid drops to intrinsic Z_{DR}. For the size spectra, the magnitude of the Z_{DR} increase is much smaller for the NS simulation than for the WS simulation. For $R = 0.5$ mm h^{-1}, the NS Z_{DR} is 0.36 dB and $D_f = 1.45$ mm as compared with 0.56 dB and $D_f = 1.75$ mm from WS. This example indicates how the width of DSD may affect the magnitude of Z_{DR} increase as well as Z_H reduction in the refreezing region. SVPs for the primary IP period indicate that the range of

maximum Z_{DR} is between 0.3 and ~0.9 dB, which is comparable to the simulated values (Fig. 10). Note that the magnitude of Z_{DR} actually decreases (by from ~0.1 to ~0.4 dB in our simulations) after all drops are frozen and is considerably less than before freezing started. This simple example suggests that the refreezing signature may be hard to observe, and the increase in Z_{DR} for ongoing freezing is likely followed by the subsequent tangible decrease as the number of larger frozen drops increases. To further validate the Marshall–Palmer (MP) model simulations, 2DVD-measured average PSDs from the primary (0645–1100 UTC; Figs. 10a,b) and secondary (1730–2130 UTC; Figs. 10c,d) ice pellet periods are sequentially frozen and presented as black lines (Z_H and Z_{DR}) in Fig. 10. Both 2DVD-measured Z_H and Z_{DR} have a similar shape as compared with the MP model when sequential freezing occurs. During the primary IP period (0645–1100 UTC), when measured PSDs were narrow ($D < 2$ mm), Z_H and Z_{DR} curves fall between MP-simulated $R = 0.1$ mm h^{-1} and $R = 0.3$ mm h^{-1}, while mean measured R_{ip} is 0.21 mm h^{-1}. During the secondary IP period (1730–2130 UTC), the
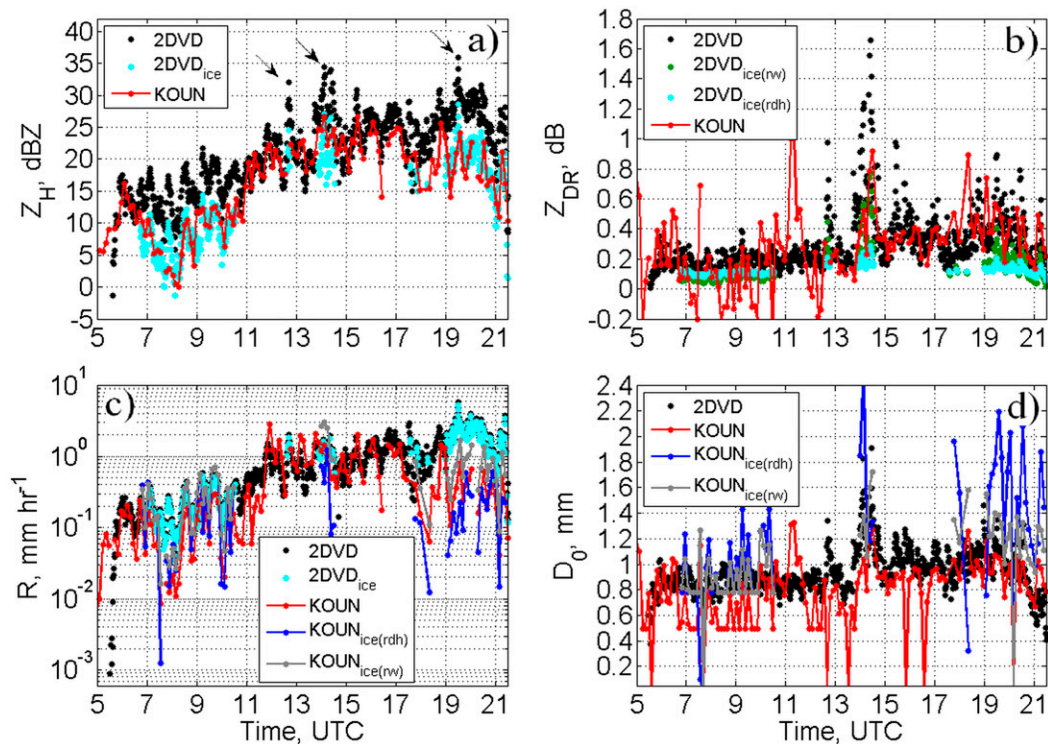
FIG. 11. Comparison of (a) Z_H, (b) Z_{DR}, and (c) rainfall rate, where the ice phase adjustments are in cyan (small dry hail aspect ratio) and green (raindrop aspect ratio) dots for 2DVD and in blue dotted (small dry hail aspect ratio) and gray dotted (raindrop aspect ratio) lines for KOUN, and (d) median volume diameter, obtained from radar DSD retrieval (KOUN) and disdrometer; black dots are 2DVD measurements (liquid phase assumption), whereas red dotted lines represent KOUN measurements and retrievals (liquid phase assumption); time series for an 0° KOUN elevation angle. Black arrows in (a) represent short periods of relatively large discrepancies between radar and 2DVD characterized as IPs.

shape of the measured Z_H and Z_{DR} curves are similar to MP simulations, but Z_{DR} falls between $R = 0.5\,\mathrm{mm\,h^{-1}}$ and $R = 1\,\mathrm{mm\,h^{-1}}$, while Z_H is higher than the one calculated for $R = 1\,\mathrm{mm\,h^{-1}}$. Mean measured $R_{ip} = 1.68\,\mathrm{mm\,h^{-1}}$, which is very close to the value expected for the MP Z_H for the same R. In general, the discrepancies in Z_{DR} are likely due to differences between measured (averaged) and MP-simulated PSD, and the choice of the aspect ratio and canting angle can highly affect Z_{DR} magnitude. Disdrometer measurements agree well with the simulations and increase confidence in the preferential drop freezing hypothesis.

e. Radar–disdrometer comparisons

Radar–disdrometer comparisons are presented in Figs. 11 and 12 for 0° and 0.41° beam elevations, respectively. In this case, the variables are Z_H and Z_{DR} and retrieved microphysical parameters R_r and D_{0r}. One should be aware of 2DVD measurement error sources: they are most frequently induced by drop splashing (Kruger and Krajewski 2002), wind effects in precipitation measurements (Nešpor et al. 2000), and

particle mismatching (Huang et al. 2010, 2015) in the case of snow. In the initial and late storm stage, the difference between radar-measured (red dotted line in Fig. 11a; 0° elevation angle) and 2DVD-calculated Z_H (assuming liquid water; black dots in Fig. 11a) is ~6–7 dB, primarily because of the difference between the refractive indices of liquid and ice hydrometeors. After replacing the dielectric constant of water with that of ice and recalculating scattering amplitudes using Rayleigh–Gans approximation for the periods from 0645 to 1100 UTC and from 1730 to 2130 UTC, the results for Z_H are in much better agreement (Fig. 11a; cyan dots), while Z_{DR} results are slightly better (Fig. 11b; cyan and green dots). For both Z_H and Z_{DR} ice phase calculations, two axes ratios are used: r_{dh} [Eq. (8)] and r_w [Eq. (9)]. The axis ratio r_{dh} is the ratio of the vertical over horizontal axis for small dry hail (Ryzhkov et al. 2011a), while r_w represents the axis ratio of the raindrops (Brandes et al. 2002). There is not a large difference between Z_H values obtained from different axis ratios (for simplicity, only cyan dots obtained from r_{dh} are shown in Fig. 11a), but Z_{DR} values are susceptible to change in
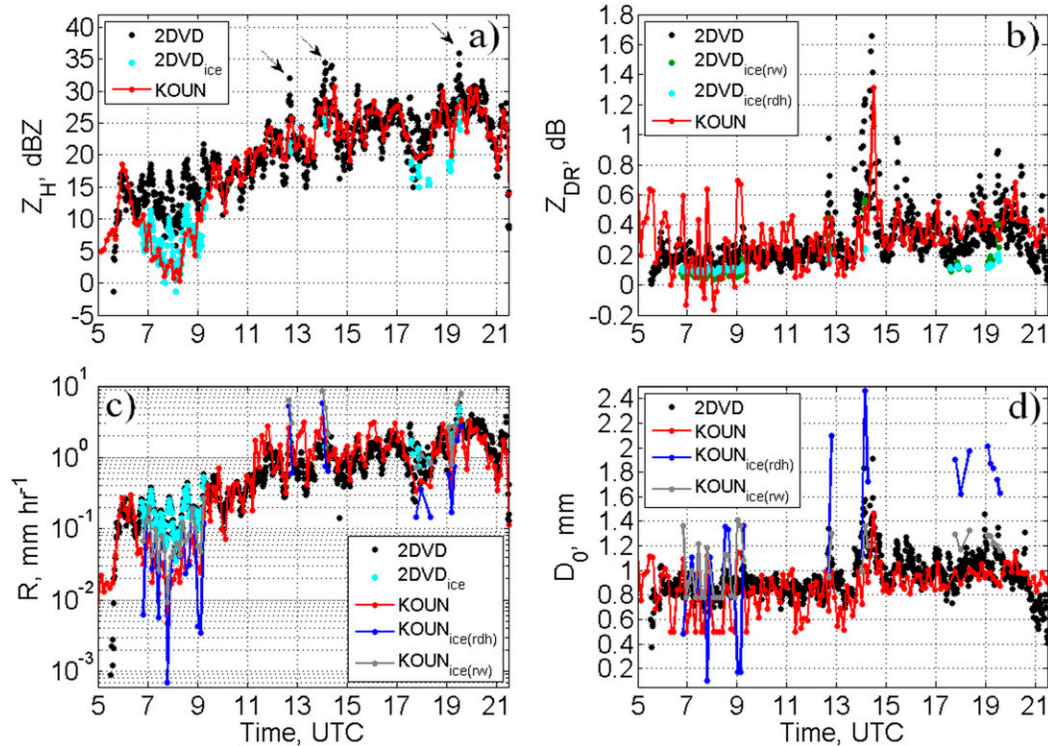
FIG. 12. As in Fig. 11, but for 0.41° KOUN elevation angle.

particle shape, as seen in Fig. 11b, where cyan dots are obtained from r_{dh} computations, and green dots are obtained from r_w computations. In the primary IP period, the values of Z_{DR} obtained through r_{dh} and r_w are comparable, but in the secondary IP periods, the r_w Z_{DR} values (green dots in Fig. 11b) are in slightly better agreement with the measured radar Z_{DR} (red dotted line in Fig. 11b). As a reminder, black dots represent 2DVD Z_{DR} computed with the dielectric constant of water and raindrop r_w axis ratio. Taking this into account, along with the RUC analysis soundings and SVPs, the observed trends in polarimetric variables are caused by the liquid–ice phase transition that characterizes ice pellet formation.

Radar-retrieved rainfall rate R_r (red dotted line in Fig. 11c) is in slightly better agreement with the disdrometer after the 2DVD ice phase adjustment (Fig. 11c; cyan dots; it is R_{ip} after the ice phase adjustment instead of R), but the relative difference is still large for the period from 0645 to 1100 UTC and approximately from 1730 to 2130 UTC. This is mostly due to the assumption that the precipitation type is rain in radar R_r (red dotted line) retrieval. After the ice phase adjustment for radar-retrieved IP rate, R_{ipr} (in Fig. 11c, blue dotted line is R_{ipr} retrieved using r_{dh}, and gray dotted line is R_{ipr} retrieved using r_w) is in better agreement with 2DVD ice phase adjustment for the primary

IP period (except for the few outliers). The variable R_{ipr} retrieved using r_w is comparable to the R_{ipr} obtained using r_{dh} but in slightly better agreement with R_{ip} from 2DVD. For later IP periods, r_{dh} R_{ipr} retrieval (blue dotted lines; Fig. 11c) degrades even more than retrieved R_r (red dotted line in Fig. 11c), while the r_w R_{ipr} values (gray dotted line; Fig. 11c) are in fairly good agreement for all IP periods. It seems that currently used, direct-radar retrieval algorithms underestimate the precipitation rate during the occurrence of ice pellets, but this could be adjusted with more suitable axis ratio and particle density relations. In addition, the low concentration of precipitation particles imposes a restriction during the ice phase periods, limiting the accuracy of DSD measurements and radar DSD retrievals. In general, the radar-retrieved and 2DVD-measured rain rates are in fair agreement; during the ice phases, there are moderate improvements for the IP periods using the raindrop axis ratios but not for the later ones if the axis ratios of dry hail are used for the ice phase adjustment. Radar-retrieved median volume diameter (red dotted line in Fig. 11d; liquid phase assumption), especially for the primary ice phase period (0645 until 1100 UTC), is noisy and with a much larger range of values relative to the 2DVD measurements. In the later stages, the two are in fair agreement, with retrieved

values slightly underestimated (D_{0r} between 0.8 and 1.2 mm). Adjusting for the ice phase, radar-retrieved D_{0r} agrees much better with the 2DVD-measured one for the primary IP period. The results from $r_w D_{0r}$ (gray dotted line; Fig. 11d) are slightly better than the ones from $r_{dh} D_{0r}$ (blue dotted line; Fig. 11d). In later IP periods, $r_{dh} D_{0r}$ retrievals substantially degrade, while the $r_w D_{0r}$ retrievals are in fair to good agreement with 2DVD.

It is very informative to take a look at radar–disdrometer comparisons at the next available radar beam elevation, 0.41°. As seen in Fig. 12a, the biggest differences between the radar-measured (red dotted line in Fig. 12a) and the 2DVD-calculated Z_H (assuming liquid water; black dots in Fig. 12a) is ~6–7 dB and occurred in the initial storm stage (0645–0920 UTC). This is primarily due to the differences between the refractive indices of liquid and ice hydrometeors. After replacing the dielectric constant of water with that of ice and recalculating scattering amplitudes using Rayleigh–Gans approximation for the period from 0645 to 0920 UTC, the results for Z_H are in much better agreement (Fig. 12a; cyan dots). This confirms that at both 0° and 0.41° radar elevations refreezing occurred, with slightly shorter duration at the 0.41° elevation. From 0645 until 0920 UTC, the radar-measured Z_{DR} is noisy, and the results obtained from r_{dh} 2DVD calculations (Fig. 12b; cyan dots) are in slightly better agreement than those obtained from r_w. In later IP periods (from 1730 to 1910 UTC), 2DVD-calculated Z_{DR} using both r_{dh} and r_w are in worse agreement with the radar than the ones calculated for pure liquid phase (black dots; Fig. 12b). This is likely due to beam smoothing of the liquid contribution because, during this period, the refreezing-level height is lower than during the initial IP period, while the melting layer is deeper and stronger. Clearly, the refreezing processes can be localized and altitude dependent and, if shallow and far from radar, are hard to detect.

Radar-retrieved rainfall rate R_r (red dotted line in Fig. 12c) is in slightly better agreement with 2DVD after the ice phase adjustment (Fig. 12c; cyan dots; it is rather R_{ip} after the ice phase adjustment instead of R), but the relative difference is still big for the period 0645–0920 UTC and approximately at 1730, 1815, and 1905 UTC. After the ice phase adjustment for radar-retrieved IP rate using the dry hail axis ratio r_{dh}, R_{ipr} (blue dotted line in Fig. 12c) is in better agreement with the 2DVD ice phase adjustment during the primary IP period (except for the few outliers) but degrades even more than retrieved R_r in later IP periods. The best agreement between radar-retrieved R_{ipr} and the one calculated from 2DVD is achieved if r_w is used for retrievals of R_{ipr}. The low concentration of precipitation particles during the ice phase periods is restricting the accuracy of DSD measurements and radar DSD retrievals. In general, the differences between radar-retrieved and 2DVD-measured rain rates are small to moderate, whereas during the ice phase there are possible improvements that depend on the choice of the ice pellet axis ratios. Radar-retrieved median volume diameter (red dotted line in Fig. 12d; liquid phase assumption), especially during the first ice phase period (0645–0920 UTC), is noisy and fluctuates much more relative to the 2DVD measurements. In the later stages, the two are in fair agreement, with the values of D_{0r} between 0.8 and 1.1 mm. The peak of the radar-retrieved D_{0r} (1.5 mm) occurred at ~1440 UTC and corresponds to relatively high values of Z_{DR} (1.5 dB) caused by few large particles. Overall, the results during the rain periods agree well. After accounting for the ice phase (in Fig. 12d, the blue dotted line using r_{dh} and gray dotted line using r_w), D_{0r} retrieval is in better agreement with 2DVD measurements in the primary IP period (except for the few outliers) but degrades substantially in the later ice pellet periods if the dry hail r_{dh} axis ratio is used.

Besides the discrepancies occurring in the two main ice phase transitions, there have been a few other short periods with relatively large differences between radar and 2DVD measurements. These periods are marked with black arrows in Figs. 11a and 12a at 1245, 1410, and 1930 UTC. The distinction with regard to the main IP periods is in the relatively larger Z_{DR} (0.4–0.8 dB) difference between the instruments (with respect to the liquid phase assumption in the 2DVD calculations; black dots in Figs. 11 and 12), along with the 4–7-dB difference in Z_H. A closer analysis of 2DVD DSD data (Fig. 5a) indicates that the concentration of the particles during these periods is slightly lower than values in adjacent times when fewer large particles are present. The jump in particle sizes is also seen in 2DVD D_0 measurements. In the SVPs from these periods, there are short episodes of weak to moderate local enhancements in Z_H, Z_{DR}, and ρ_{hv} at the times of interest. This is indicative of rain. Since the particles classified with 2DVD are ice pellets, the differences most likely originate from the much larger area over which the radar data are averaged (20° in azimuth for SVPs) or because of the short temporal scales of the refreezing episodes.

5. Discussion

An observational study of a 20 January 2007 winter precipitation event using S-band polarimetric KOUN radar data and OU 2DVD measurements in Oklahoma is presented. The case is classified as a wintery mix of ice pellet and rain/freezing rain periods. RUC analysis and RASS profiles provided insight into environmental

conditions, while storm structure and evolution are studied using the polarimetric radar and disdrometer observations. The PPI of Z_H, Z_{DR}, and ρ_{hv} revealed the morphology of the storm. Refreezing occurred locally at a distance of 30–40 km from the radar and exhibited a patchy structure of weakly enhanced Z_{DR} (up to 0.2–0.3 dB) and reduced Z_H and ρ_{hv} values.

Radar-measured vertical profiles and time evolution of Z_H, Z_{DR}, and ρ_{hv} over the disdrometer site are extracted from volume scans and analyzed. Radar vertical profiles presented in somewhat enhanced vertical resolution show a reduction in Z_H and ρ_{hv} and very weak enhancement in Z_{DR} as rain on its descent is transitioning to ice pellets. Coarser vertical resolution of regular profiles hints at some of the refreezing episodes but misses other signatures and hence is deficient relative to the EVPs. The EVPs can moderately improve vertical resolution and continuity and therefore better isolate the refreezing signatures. A novel technique of polarimetric radar data processing/viewing, the SVPs at lowest elevations, is used for semiquantitative analysis. This technique improves the diagnostics of localized refreezing at locations away from the radar because it enhances vertical resolution. In the case of homogeneous precipitation over large areas, the whole profile (from top to bottom) can be interpreted for microphysical inferences within the vertical column. But, in horizontally nonhomogeneous precipitation, as was the case in our study, the SVP is not representative of the true vertical column. Nonetheless, incremental values centered at a fixed height can represent well the actual variables at the corresponding range. The time evolutions of the DSD, mass, reflectivity, and differential reflectivity distributions obtained with the 2DVD are examined. These generally show narrower distributions and lower particle concentrations during the ice phase periods than during rain periods. Polarimetric radar variables were calculated from 2DVD data and compared with KOUN radar measurements, while radar-retrieved DSDs are compared with the disdrometer measurements. Polarimetric variables Z_H and Z_{DR}, as well as microphysical parameters of radar-retrieved DSDs, rainfall rate (R_r), and median volume diameter (D_{0r}), generally agree well with 2DVD calculations/measurements, although discrepancies occur during the time of the ice phase if this phase transition is not recognized.

Estimates of Z_H from 2DVD in which the correct precipitation phase is assumed significantly improve agreement with radar-measured Z_H. However, improvement in Z_{DR} is marginal. This is because ice pellets and small raindrops have similar values of Z_{DR}. Using a novel approach, the SVPs at low elevations

and an in situ instrument (2DVD) make it possible to extend remote measurements from the ground into the area above. In this case, in situ observations and remote radar measurements are consistent with the observations of ice pellets.

6. Summary

The following summarizes principal findings of this paper:

1) Recognition of ice pellets with the polarimetric radar in localized areas up to about 50 km away from the radar is challenging. It is doable if the melting layer and refreezing layer are spaced by more than the beamwidth, and refreezing is not below the radar horizon. Benefiting from previous observations and collocated 2DVD and other measurements, we were able not only to confirm the refreezing signatures but also to quantify the amount of frozen precipitation.

2) Slow-falling (1–3 m s^{-1}) ice pellets were readily recognized in the 2DVD data. The rugged shapes of the pellets larger than 1.5 mm made them easily detectable at any fall speed. Because small drops freeze faster than large ones, the presence of large pellets indicates that the smaller ones must be frozen too. This facilitated the overall discrimination.

3) The patchy refreezing structure in PPIs is in contrast to Ryzhkov et al.'s (2011b) and Kumjian et al.'s (2013) observations where the increase in Z_{DR} and the reduction in ρ_{hv} have ringlike structures, while a reduction in Z_H (by about 7 dB, same as in our case) was more gradual. The differences can be due to the locality of our measurements, where the refreezing processes occurred much closer to the ground. Polarimetric signature of local enhancement in Z_{DR} and reduction in both Z_H and ρ_{hv} is the same, except the magnitude of Z_{DR} enhancement due to refreezing of smaller sizes (0.1–0.3 dB) is lower in our study. This is due to smaller particle size spectra during the ice phase.

4) Environmental conditions, such as the presence of melting and freezing layers and also freezing temperatures not colder than $-3.5°C$ within refreezing zones, indicated that preferential freezing of smaller drops is most likely the mechanism that produces the refreezing polarimetric signatures.

5) The magnitudes of Z_H, Z_{DR}, and ρ_{hv} per se are not sufficient for identifying refreezing, but their spatial and temporal changes reveal the locations of refreezing.

6) Simulations of preferential drop freezing suggest complexity in the refreezing signatures, such as

dependence on the width of the particle size spectra, and particle sizes (smaller drops freeze faster), in conjunction with the environmental conditions (e.g., temperature and relative humidity). The simulated refreezing signature of Z_{DR} is especially instructive: Z_{DR} increases during preferential freezing, but after larger drops start to freeze, it drops substantially (depending on the particle size), as confirmed by 2DVD measurements. This indirectly indicates that the refreezing signatures are altitude (because of temperature) dependent and that the enhancement of the Z_{DR} may be followed by a substantial reduction over a small vertical distance.

REFERENCES

Atlas, D., C. W. Ulbrich, F. D. Marks Jr., E. Amitai, and C. R. Williams, 1999: Systematic variation of drop size and radar-rainfall relations. *J. Geophys. Res.*, **104**, 6155–6169, doi:10.1029/1998JD200098.

Brandes, E. A., G. Zhang, and J. Vivekanandan, 2002: Experiments in rainfall estimation with a polarimetric radar in a subtropical environment. *J. Appl. Meteor.*, **41**, 674–685, doi:10.1175/1520-0450(2002)041<0674:EIREWA>2.0.CO;2.

——, ——, and ——, 2003: An evaluation of a drop distribution–based polarimetric radar rainfall estimator. *J. Appl. Meteor.*, **42**, 652–660, doi:10.1175/1520-0450(2003)042<0652:AEOADD>2.0.CO;2.

——, ——, and ——, 2004a: Comparison of polarimetric radar drop size distribution retrieval algorithms. *J. Atmos. Oceanic Technol.*, **21**, 584–598, doi:10.1175/1520-0426(2004)021<0584:COPRDS>2.0.CO;2.

——, ——, and ——, 2004b: Drop size distribution retrieval with polarimetric radar: Model and application. *J. Appl. Meteor.*, **43**, 461–475, doi:10.1175/1520-0450(2004)043<0461:DSDRWP>2.0.CO;2.

——, K. Ikeda, G. Zhang, M. Schönhuber, and R. M. Rasmussen, 2007: A statistical and physical description of hydrometeor distributions in Colorado snowstorms using a video disdrometer. *J. Appl. Meteor. Climatol.*, **46**, 634–650, doi:10.1175/JAM2489.1.

Bringi, V. N., V. Chandrasekar, J. Hubbert, E. Gorgucci, W. L. Randeu, and M. Schoenhuber, 2003: Raindrop size distribution in different climatic regimes from disdrometer and dual-polarized radar analysis. *J. Atmos. Sci.*, **60**, 354–365, doi:10.1175/1520-0469(2003)060<0354:RSDIDC>2.0.CO;2.

Bukovčić, P., D. Zrnić, and G. Zhang, 2015: Convective–stratiform separation using video disdrometer observations in central Oklahoma—The Bayesian approach. *Atmos. Res.*, **155**, 176–191, doi:10.1016/j.atmosres.2014.12.002.

Cao, Q., G. Zhang, E. Brandes, T. Schuur, A. Ryzhkov, and K. Ikeda, 2008: Analysis of video disdrometer and polarimetric radar data to characterize rain microphysics in Oklahoma. *J. Appl. Meteor. Climatol.*, **47**, 2238–2255, doi:10.1175/2008JAMC1732.1.

Cortinas, J. V., Jr., B. C. Bernstein, C. C. Robbins, and J. W. Strapp, 2004: An analysis of freezing rain, freezing drizzle, and ice pellets across the United States and Canada: 1976–90. *Wea. Forecasting*, **19**, 377–390, doi:10.1175/1520-0434(2004)019<0377:AAOFRF>2.0.CO;2.

Doviak, R. J., and D. S. Zrnić, 1993: *Doppler Radar and Weather Observations.* 2nd ed. Dover Publications, Inc., 592 pp.

Gibson, S. R., and R. E. Stewart, 2007: Observations of ice pellets during a winter storm. *Atmos. Res.*, **85**, 64–76, doi:10.1016/j.atmosres.2006.11.004.

——, ——, and W. Henson, 2009: On the variation of ice pellet characteristics. *J. Geophys. Res.*, **114**, D09207, doi:10.1029/2008JD011260.

Goddard, J. W. F., S. M. Cherry, and V. N. Bringi, 1982: Comparison of dual-polarization radar measurements of rain with ground-based disdrometer measurements. *J. Appl. Meteor.*, **21**, 252–256, doi:10.1175/1520-0450(1982)021<0252:CODPRM>2.0.CO;2.

Huang, G.-J., V. N. Bringi, R. Cifelli, D. Hudak, and W. A. Petersen, 2010: A methodology to derive radar reflectivity–liquid equivalent snow rate relations using C-band radar and a 2D video disdrometer. *J. Atmos. Oceanic Technol.*, **27**, 637–651, doi:10.1175/2009JTECHA1284.1.

——, ——, D. Moisseev, W. A. Petersen, L. Bliven, and D. Hudak, 2015: Use of 2D-video disdrometer to derive mean density–size and Z_e–SR relations: Four snow cases from the light precipitation validation experiment. *Atmos. Res.*, **153**, 34–48, doi:10.1016/j.atmosres.2014.07.013.

Ikeda, K., E. A. Brandes, and R. M. Rasmussen, 2005a: Notes and correspondence: Polarimetric radar observation of multiple freezing levels. *J. Atmos. Sci.*, **62**, 3624–3636, doi:10.1175/JAS3556.1.

——, ——, G. Zhang, and S. A. Rutledge, 2005b: Observations of winter storms with a 2-D video disdrometer and polarimetric radar. *32nd Conf. on Radar Meteorology*, Albuquerque, NM, Amer. Meteor. Soc., P11R.14. [Available online at https://ams.confex.com/ams/32Rad11Meso/webprogram/Paper97054.html.]

Islam, T., M. A. Rico-Ramirez, M. Thurai, and D. Han, 2012: Characteristics of raindrop spectra as normalized gamma distribution from a Joss–Waldvogel disdrometer. *Atmos. Res.*, **108**, 57–73, doi:10.1016/j.atmosres.2012.01.013.

Kruger, A., and W. F. Krajewski, 2002: Two-dimensional video disdrometer: A description. *J. Atmos. Oceanic Technol.*, **19**, 602–617, doi:10.1175/1520-0426(2002)019<0602:TDVDAD>2.0.CO;2.

Kumjian, M. R., and A. D. Schenkman, 2014: The curious case of ice pellets over middle Tennessee on 1 March 2014. *J. Oper. Meteor.*, **2**, 209–213, doi:10.15191/nwajom.2014.0217.

——, A. V. Ryzhkov, H. D. Reeves, and T. J. Schuur, 2013: A dual-polarization radar signature of hydrometeor refreezing in winter storms. *J. Appl. Meteor. Climatol.*, **52**, 2549–2566, doi:10.1175/JAMC-D-12-0311.1.

Nagumo, N., and Y. Fujiyoshi, 2015: Microphysical properties of slow-falling and fast-falling ice pellets formed by freezing

associated with evaporative cooling. *Mon. Wea. Rev.*, **143**, 4376–4392, doi:10.1175/MWR-D-15-0054.1.

Nešpor, V., W. F. Krajewski, and A. Kruger, 2000: Wind-induced error of raindrop size distribution measurement using a two-dimensional video disdrometer. *J. Atmos. Oceanic Technol.*, **17**, 1483–1492, doi:10.1175/1520-0426(2000)017<1483:WIEORS>2.0.CO;2.

Niu, S., X. Jia, J. Sang, X. Liu, C. Lu, and Y. Liu, 2010: Distributions of raindrop sizes and fall velocities in a semiarid plateau climate: Convective versus stratiform rains. *J. Appl. Meteor. Climatol.*, **49**, 632–645, doi:10.1175/2009JAMC2208.1.

Raga, G. B., R. E. Stewart, and N. R. Donaldson, 1991: Microphysical characteristics through the melting region of a midlatitude winter storm. *J. Atmos. Sci.*, **48**, 843–855, doi:10.1175/1520-0469(1991)048<0843:MCTTMR>2.0.CO;2.

Ryzhkov, A., G. Zhang, S. Luchs, and L. Ryzhkova, 2008: Polarimetric characteristics of snow measured by radar and 2D video disdrometer. *Proc. Fifth European Conf. on Radar in Meteorology and Hydrology*, Helsinki, Finland, European Organisation for the Exploitation of Meteorological Satellites, 4 pp.

——, M. Pinsky, A. Pokrovsky, and A. Khain, 2011a: Polarimetric radar observation operator for a cloud model with spectral microphysics. *J. Appl. Meteor. Climatol.*, **50**, 873–894, doi:10.1175/2010JAMC2363.1.

——, H. D. Reeves, T. J. Schuur, M. R. Kumjian, and D. S. Zrnic, 2011b: Investigations of polarimetric radar signatures in winter storms and their relation to aircraft icing and freezing rain. *35th Conf. on Radar Meteorology*, Pittsburgh, PA, Amer. Meteor. Soc., 197. [Available online at https://ams.confex.com/ams/35Radar/webprogram/Paper191245.html.]

——, P. Zhang, H. Reeves, M. Kumjian, T. Tschallener, S. Trömel, and C. Simmer, 2016: Quasi-vertical profiles—A new way to look at polarimetric radar data. *J. Atmos. Oceanic Technol.*, **33**, 551–562, doi:10.1175/JTECH-D-15-0020.1.

Schuur, T. J., A. V. Ryzhkov, D. S. Zrnić, and M. Schönhuber, 2001: Drop size distributions measured by a 2D video disdrometer: Comparison with dual-polarization radar data. *J. Appl. Meteor.*, **40**, 1019–1034, doi:10.1175/1520-0450(2001)040<1019:DSDMBA>2.0.CO;2.

Tao, W.-K., S. Lang, X. Zeng, S. Shige, and Y. Takayabu, 2010: Relating convective and stratiform rain to latent heating. *J. Climate*, **23**, 1874–1893, doi:10.1175/2009JCLI3278.1.

Thurai, M., G. J. Huang, V. N. Bringi, W. L. Randeu, and M. Schönhuber, 2007: Drop shapes, model comparisons, and calculations of polarimetric radar parameters in rain. *J. Atmos. Oceanic Technol.*, **24**, 1019–1032, doi:10.1175/JTECH2051.1.

——, C. R. Williams, and V. N. Bringi, 2014: Examining the correlations between drop size distribution parameters using data from two side-by-side 2D-video disdrometers. *Atmos. Res.*, **144**, 95–110, doi:10.1016/j.atmosres.2014.01.002.

Tokay, A., and D. A. Short, 1996: Evidence from tropical raindrop spectra of the origin of rain from stratiform versus convective clouds. *J. Appl. Meteor.*, **35**, 355–371, doi:10.1175/1520-0450(1996)035<0355:EFTRSO>2.0.CO;2.

Trapp, R. J., D. M. Schultz, A. V. Ryzhkov, and R. L. Holle, 2001: Multiscale structure and evolution of an Oklahoma winter precipitation event. *Mon. Wea. Rev.*, **129**, 486–501, doi:10.1175/1520-0493(2001)129<0486:MSAEOA>2.0.CO;2.

Ulbrich, C. W., 1983: Natural variations in the analytical form of the raindrop size distribution. *J. Climate Appl. Meteor.*, **22**, 1764–1775, doi:10.1175/1520-0450(1983)022<1764:NVITAF>2.0.CO;2.

Williams, C. R., and Coauthors, 2014: Describing the shape of raindrop size distributions using uncorrelated raindrop mass spectrum parameters. *J. Appl. Meteor. Climatol.*, **53**, 1282–1296, doi:10.1175/JAMC-D-13-076.1.

Yuter, S. E., D. E. Kingsmill, L. B. Nance, and M. Löffler-Mang, 2006: Observations of precipitation size and fall speed characteristics within coexisting rain and wet snow. *J. Appl. Meteor. Climatol.*, **45**, 1450–1464, doi:10.1175/JAM2406.1.

——, D. A. Stark, M. T. Bryant, B. A. Colle, L. B. Perry, J. Blaes, J. Wolfe, and G. Peters, 2008: Forecasting and characterization of mixed precipitation events using the MicroRainRadar. *Proc. Fifth European Conf. on Radar in Meteorology and Hydrology*, Helsinki, Finland, European Organisation for the Exploitation of Meteorological Satellites. [Available online at http://www4.ncsu.edu/~seyuter/pdfs/080505YuteretalERAD.pdf.]

Zhang, G., 2016: *Weather Radar Polarimetry*. CRC Press, 304 pp.

——, J. Vivekanandan, and E. Brandes, 2001: A method for estimating rain rate and drop size distribution from polarimetric radar measurements. *IEEE Trans. Geosci. Remote Sens.*, **39**, 830–841, doi:10.1109/36.917906.

——, ——, ——, R. Meneghini, and T. Kozu, 2003: The shape–slope relation in observed gamma raindrop size distributions: Statistical error or useful information? *J. Atmos. Oceanic Technol.*, **20**, 1106–1119, doi:10.1175/1520-0426(2003)020<1106:TSRIOG>2.0.CO;2.

——, J. Sun, and E. A. Brandes, 2006: Improving parameterization of rain microphysics with disdrometer and radar observations. *J. Atmos. Sci.*, **63**, 1273–1290, doi:10.1175/JAS3680.1.

——, M. Xue, Q. Cao, and D. Dawson, 2008: Diagnosing the intercept parameter for exponential raindrop size distribution based on video disdrometer observations: Model development. *J. Appl. Meteor. Climatol.*, **47**, 2983–2992, doi:10.1175/2008JAMC1876.1.

——, S. Luchs, A. Ryzhkov, M. Xue, L. Ryzhkova, and Q. Cao, 2011: Winter precipitation microphysics characterized by polarimetric radar and video disdrometer observations in central Oklahoma. *J. Appl. Meteor. Climatol.*, **50**, 1558–1570, doi:10.1175/2011JAMC2343.1.